Common-path off-axis single-pixel holographic imaging

Yoneda, Naru
Saita, Yusuke
Nomura, Takanori

(Citation)
Optics Express,30(11):18134-18144

(Issue Date)
2022-05-23

(Resource Type)
journal article

(Version)
Version of Record

Research Article | Vol. 30, No. 11 / 23 May 2022 / Optics Express 18134
Optics EXPRESS

Common-path off-axis single-pixel holographic imaging

NARU YONEDA,[1,2,3,*] YUSUKE SAITA,[4] AND TAKANORI NOMURA[4]

[1] *Graduate School of Systems Engineering, Wakayama University, 930 Sakaedani, Wakayama, 640-8510, Japan*
[2] *Research Fellow of the Japan Society for the Promotion of Science, 5-3-1 Kojimachi, Chiyoda, Tokyo 102-0083, Japan*
[3] *Current address: Graduate School of System Informatics, Department of System Science, Kobe University, Rokkodai 1-1, Nada, Kobe 657-8501, Japan*
[4] *Faculty of Systems Engineering, Wakayama University, 930 Sakaedani, Wakayama, 640-8510, Japan*
[*] *yoneda.naru@port.kobe-u.ac.jp*

Abstract: Common-path off-axis single-pixel holographic imaging (COSHI) is proposed to obtain complex amplitude information using an in-line interferometer and a single-pixel (point-like) detector. COSHI is more robust to disturbances such as vibration than the conventional single-pixel digital holography technique because of its common-path configuration. In addition, the number of measurements can be reduced due to COSHI's reconstruction process based on the Fourier fringe analysis. In COSHI, an off-axis digital hologram can be obtained using the structured patterns composed of Hadamard basis patterns and stationary tilted phase distribution. Interestingly, COSHI's space bandwidth is larger than of the conventional off-axis digital holography because COSHI does not reconstruct the self-correlation term of an object. The proposed method is theoretically confirmed and numerical and experimental results show its feasibility.

1. Introduction

Single-pixel imaging (SPI) is an attractive technique since it detects two-dimensional (2D) images without a 2D image sensor [1–4]. Over the past few decades, SPI has been applied to various applications such as optical encryption [5], three-dimensional (3D) imaging [6], microscopy [7], remote sensing [8], terahertz imaging [9], tomography [10], broadcast imaging [11], spectral imaging [12], and polarization imaging [13]. In addition, phase imaging is also achieved in SPI. The phase imaging techniques in SPI can be classified as either noninterferometric or interferometric methods. In the noninterferometric methods, the transport of intensity equation (TIE) [14,15] has been applied to computational ghost imaging (CGI) [16]. However, TIE-based CGI can only reconstruct the weak phase object following Teague's assumption. A differential phase contrast (DPC) method has been applied to CGI, which was proposed as a noninterferometric SPI [17]. The measurable phase difference in DPC-based CGI, similar to TIE-based CGI, is restricted by the constraint imposing weak object approximation. Single-pixel ptychography, which is a noninterferometric SPI, can mitigate the phase difference problem [18]. However, an iterative phase retrieval process is required in the ptychographic approach, which imposes a high computational cost. K. Komuro *et al.* have proposed deep ghost phase imaging (DGPI) for improving the image quality of TIE-based CGI using a deep neural network [19]. Although DGPI mitigates the problem of TIE-based CGI, a large amount of measurements is required to obtain the data sets for the neural network.

On the other hand, various interferometric SPI techniques have been proposed. Clemente, *et al.* proposed digital ghost holography (DGH) [20] that can detect phase information with

#455166 https://doi.org/10.1364/OE.455166
Journal © 2022 Received 31 Jan 2022; revised 30 Apr 2022; accepted 2 May 2022; published 11 May 2022

Optics EXPRESS

a Mach-Zehnder interferometer. Ghost Mach-Zehnder interferometry has also been proposed [21]. Moreover, a Michelson interferometer can be used in single-pixel digital holography (SPDH) [22]; accordingly, the patterns do not have to illuminate an object directly. SPDH has been applied in various applications, such as multi-color [23] and biological imaging [24]. SPDH can achieve a high sampling rate using a digital micromirror device [25]. However, the requirement of a two-beam interferometer makes the optical setup bulky and complicated. In addition, DGH and SPDH require three or four times the number of measurements compared with conventional SPI because they are based on the phase-shifting technique [26]. Various common-path configurations have been proposed [27–31] to overcome the optical setup issue. Particularly, single-point holography (SPH) [27,28] can reconstruct complex information using a common-path setup and a single-pixel (point like) detector. In SPH, complex amplitude information can be obtained by extracting a zeroth order diffracted light in a Fourier plane. The use of the zeroth order diffracted light is also proposed in optical scanning holography [32–34], GI [35], Hadamard SPI [36], and single-pixel wavefront sensor [37]. However, there is still a problem with the number of measurements due to the phase-shifting.

In this study, common-path off-axis single-pixel holographic imaging (COSHI) is proposed to obtain complex amplitude information with an in-line interferometer and a single-pixel (point-like) detector. Similar to SPH, COSHI is more robust to disturbances such as vibration than conventional DGH and SPDH. In addition, the number of measurements can be reduced compared with other common-path techniques such as SPH owing to the reconstruction process based on the Fourier fringe analysis (FFA) [38] rather than the phase-shifting method. In COSHI, off-axis digital holograms can be obtained using the structured patterns composed of Hadamard basis patterns and a stationary tilted phase distribution. These structured patterns are easily generated using a phase-type spatial light modulator (SLM) and its polarization dependence. The off-axis digital holograms are obtained through the reconstruction process which is the same as the conventional SPI. Interestingly, COSHI's space bandwidth is larger than the conventional off-axis digital holography because COSHI does not reconstruct the self-correlation term of an object.

2. Principle

Figure 1 shows the schematic of COSHI. Structured phase patterns are used for illumination in COSHI. The structured patterns are composed of Hadamard basis patterns and a stationary tilted phase distribution. Because the Hadamard basis patterns are composed of 1 and -1, the Hadamard basis patterns are generated with the phase patterns composed of 0 and π. Therefore, the distributions of the sum between the Hadamard basis patterns and a tilted phase distribution are generated as pure phase distributions. The structured patterns are sequentially displayed on a phase-type SLM such as liquid crystal on silicon (LCoS) SLM. A diagonally polarized plane wave enters the SLM and the horizontal or vertical component is modulated by the SLM. In this explanation, it is supposed that the SLM modulates the horizontal polarized component. Thus, the vertical component transmits the SLM. These orthogonal components are projected to an object plane with a 4-f setup. In the 4-f setup, a polarizer is inserted in front of the object to align these polarized components. This polarization-based illumination technique is frequently used in SPI [39–41]. Through the process, the structured patterns and the plane wave are simultaneously illuminated to the object. The complex amplitude distribution at the object plane is described as follows:

$$f(x,y) = O(x,y)\left\{A_{\mathrm{p}} m_j(x,y) l(x,y) + A_{\mathrm{s}}\right\}, \tag{1}$$

where $O(x,y)$, A_{p}, A_{s}, $m_j(x,y)$, and $l(x,y)$ are the complex amplitude distribution of the object, polarization components of vertical and horizontal components, Hadamard patterns with $j = 1, 2, \ldots, N$, and a stationary tilted phase distribution, respectively. The polarization dependence of the object is omitted in this description for simplicity. If the objects are anisotropic,

Optics EXPRESS

the polarization dependence can be considered using the Jones matrix. The diffracted light from the object is Fourier transformed by a lens and is detected using a single-pixel (point-like) detector. The detector is easily constructed using a pinhole and extracts a DC component. The detected intensity is described as follows:

$$\begin{aligned} I_j &= \left| \iint f(x,y)\exp\left\{-i2\pi(\mu x+\nu y)\right\} dxdy \Big|_{\mu=\nu=0} \right|^2 \\ &= \left| \iint f(x,y)dxdy \right|^2 \\ &= \left| \iint O(x,y)\left\{A_\mathrm{p} m_j(x,y)l(x,y)+A_\mathrm{s}\right\} dxdy \right|^2, \end{aligned} \tag{2}$$

where μ and ν are spatial frequency along x and y axes. Note that if the pinhole size is mismatched or the pinhole position is displaced, the relation of Eq. (2) is not satisfied. The effects of the pinhole size and the position are evaluated in discussion. Equation (2) can be expanded as

$$I_j = \left| \iint A_\mathrm{p} O(x,y)m_j(x,y)l(x,y)dxdy + \iint A_\mathrm{s} O(x,y)dxdy \right|^2. \tag{3}$$

In Eq. (3), the second term on the right hand side can be regarded as a constant R because the term is independent of $m_j(x,y)$. Therefore, Eq. (3) can be rewritten as follows:

$$\begin{aligned} I_j &= \left| \iint A_\mathrm{p} O(x,y)m_j(x,y)l(x,y)dxdy + R \right|^2 \\ &= \left| \iint A_\mathrm{p} O(x,y)m_j(x,y)l(x,y)dxdy \right|^2 + |R|^2 + R^* \iint A_\mathrm{p} O(x,y)m_j(x,y)l(x,y)dxdy \\ &+ R\left\{ \iint A_\mathrm{p} O(x,y)m_j(x,y)l(x,y)dxdy \right\}^*, \end{aligned} \tag{4}$$

where * indicates the complex conjugate. Since the Hadamard basis patterns are real functions composed of 1 and -1, $m_j(x,y) = m_j^*(x,y)$. The third and fourth terms on the right hand side of Eq. (4) are combined into one term and Eq. (4) is rewritten as follows:

$$\begin{aligned} I_j &= \left| \iint A_\mathrm{p} O(x,y)m_j(x,y)l(x,y)dxdy \right|^2 + |R|^2 \\ &\quad + \iint m_j(x,y)\left[R^* A_\mathrm{p} O(x,y)l(x,y) + \left\{R^* A_\mathrm{p} O(x,y)l(x,y)\right\}^*\right] dxdy \\ &= I_{\mathrm{S}j} + I_{\mathrm{R}j} + I_{\mathrm{AC}j}, \end{aligned} \tag{5}$$

where

$$\begin{aligned} I_{\mathrm{S}j} &= \left| \iint A_\mathrm{p} O(x,y)m_j(x,y)l(x,y)dxdy \right|^2 \\ I_{\mathrm{R}j} &= |R|^2 = \left| \iint A_\mathrm{s} O(x,y)dxdy \right|^2 \\ I_{\mathrm{AC}j} &= \iint m_j(x,y)\left[R^* A_\mathrm{p} O(x,y)l(x,y) + \left\{R^* A_\mathrm{p} O(x,y)l(x,y)\right\}^*\right] dxdy. \end{aligned}$$

Interestingly, the detected intensity can be divided into three terms, and I_{ACj} is equivalent to the interference term. Therefore, the complex amplitude distribution of the object can be obtained as the detected intensity.

Optics EXPRESS

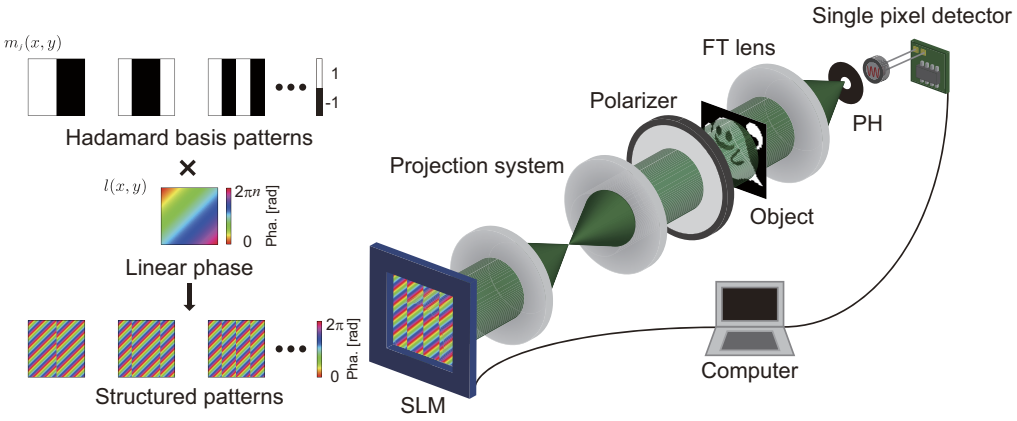

Fig. 1. Schematic diagram of COSHI. SLM, Spatial Light Modulator; FT, Fourier transform; PH, Pinhole.

In COSHI, the reconstruction process is almost the same as that in the conventional SPI. The reconstructed distribution is calculated from the sum of $m_j(x,y)$ weighted with I_j, which is described as follows:

$$\begin{aligned} H(x,y) =& \frac{1}{N}\sum_{j=1}^{N} m_j(x,y) I_j \\ =& \frac{1}{N}\sum_{j=1}^{N} m_j(x,y)(I_{\mathrm{S}j} + I_{\mathrm{R}j} + I_{\mathrm{AC}j}) \\ =& \frac{1}{N}\sum_{j=1}^{N} m_j(x,y)(I_{\mathrm{S}j} + I_{\mathrm{R}j}) + R^* A_{\mathrm{p}} O(x,y) l(x,y) + \left\{R^* A_{\mathrm{p}} O(x,y) l(x,y)\right\}^*, \end{aligned} \tag{6}$$

where N is the number of the Hadamard basis patterns. The third and fourth terms on the right hand side of Eq. (6) can be reconstructed because these terms are a linear superposition of the Hadamard basis patterns $m_j(x,y)$ weighted with $I_{\mathrm{AC}j}$. Equation (6) indicates that the reconstructed distribution of COSHI figures an off-axis hologram. In Eq. (6), the first term on the right hand side can be neglected by subtracting the post calculated distribution. Since $I_{\mathrm{AC}j}$ is the component for the interference term, the mean value of $I_{\mathrm{AC}j}$ is almost 0. Therefore, $\frac{1}{N}\sum_{j=1}^{N}(I_{\mathrm{S}j} + I_{\mathrm{R}j}) \approx \bar{I}$, where $\bar{I}$ is the ensemble average of $I_j (j = 1, 2, \ldots, N)$. To remove the first term on the right hand side in Eq. (6), the approximation of

$$\frac{1}{N}\sum_{j=1}^{N} m_j(x,y)(I_{\mathrm{S}j} + I_{\mathrm{R}j}) \approx \frac{\bar{I}}{N}\sum_{j=1}^{N} m_j(x,y) \tag{7}$$

is used. By subtracting $\frac{\bar{I}}{N}\sum_{j=1}^{N} m_j(x,y)$ from Eq. (6), the interference term is obtained and is described as follows:

$$\begin{aligned} H'(x,y) =& H(x,y) - \frac{\bar{I}}{N}\sum_{j=1}^{N} m_j(x,y) \\ \approx& R^* A_{\mathrm{p}} O(x,y) l(x,y) + \left\{R^* A_{\mathrm{p}} O(x,y) l(x,y)\right\}^*. \end{aligned} \tag{8}$$

Note that since Eq. (8) has the approximation, the approximation effect is evaluated in the discussion. This subtraction process is similar to the one in the correlation function in CGI [2,16].

Optics EXPRESS

Note that COSHI has a larger space bandwidth than the conventional off-axis digital holographic technique because the right-hand side of Eq. (8) does not contain the self-correlation term of the object. The complex amplitude distribution of the object can be obtained through the FFA. The process of the FFA is shown in Fig. 2. Firstly, the reconstructed interference distribution $H'(x, y)$ is Fourier transformed. Secondly, the desired spectrum is extracted using a filter function and is shifted to the center position. Finally, the extracted spectrum is inverse Fourier transformed and the complex amplitude distribution of the object can be obtained. Note that when the object is placed at the defocus position, i.e., shifted away from the front focal plane of the Fourier transform lens, the complex amplitude distribution of the defocused object is obtained. Therefore, by using the back propagation algorithm to the complex amplitude distribution, we can obtain the distribution at the object plane.

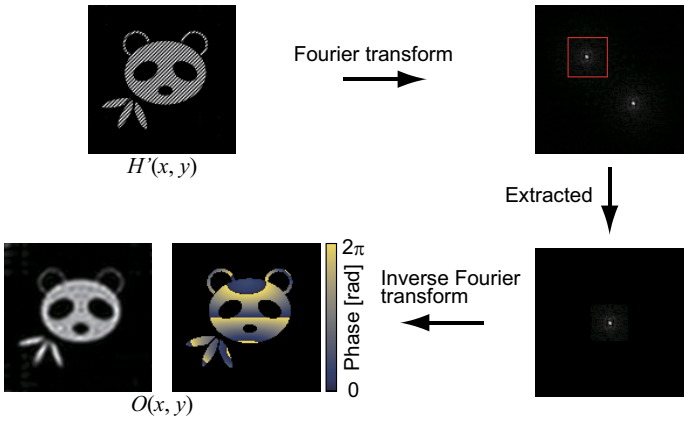

Fig. 2. The process of the FFA.

3. Proof-of-principle experiment

A proof-of-principle experiment was demonstrated to confirm the feasibility of the proposed method. The optical setup and the parameters are shown in Fig. 3. The light source is a green fiber laser (MPB Communications, Inc., VFL-P-500). The collimated beam through a spatial filter illuminates an SLM (Hamamatsu Photonics K.K. X13138-01). The center region of the SLM with 128×128 is used for the illumination patterns. Since the number of structured patterns are 128×128, the number of measurements is $128 \times 128 = 16384$. The structured illumination patterns are projected to an object with a 4-f optical setup composed by lens 2 and 3. The transmitted beam is Fourier transformed by lens 4 and is detected by a single-pixel detector composed of a pinhole (Thorlabs, Inc., P40D) and a photodiode (Hamamatsu K.K. C10439-03). The measured currents were quantized by a 16-bit analog-to-digital converter (Hamamatsu K.K. C10475). The sampling speed is limited, since the sampling rate of the analog-to-digital converter is 20 Hz. In this experiment, the sampling rate is set to 5 Hz to reduce the effect of SLM fluctuations. The diameter of the pinhole is 40μm, which is determined by the numerical aperture of lens 4 ($\frac{\lambda}{2\text{N.A.}} = 82.1\mu$m). In the FFA, a rect function is used as a filter function. The filter size is set to 1.3 mm $\times$1.3 mm. The spatial frequency of the linear phase along x and y directions is 1203 [1/m].

The target phase distributions are shown in Figs. 4(a1)–4(a3). To evaluate whether any distribution can be measured, we used three different phase distributions. These phase distributions in Figs. 4(a1)–4(a3) are generated by the Zernike polynomials. The phase distributions are displayed to the SLM with the structured patterns, which is assumed as the complex amplitude

Optics EXPRESS

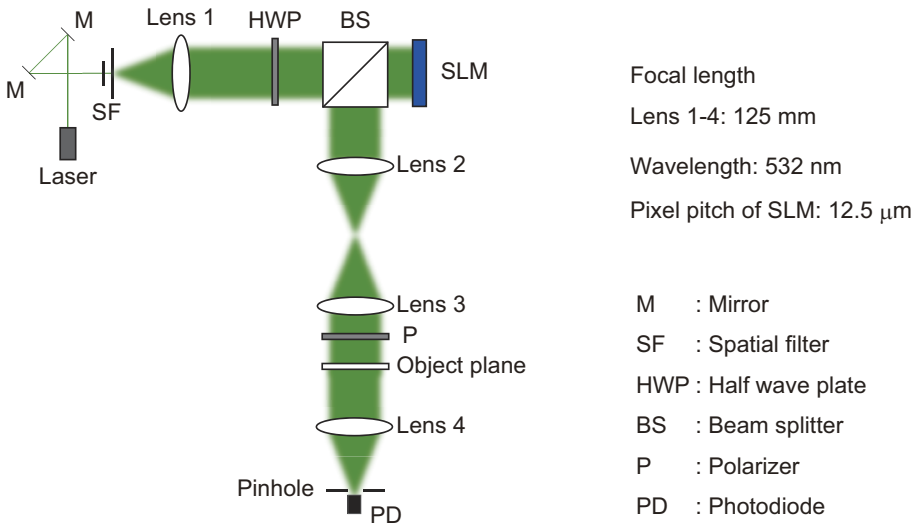

Fig. 3. The optical setup and the parameter for the experiment.

distributions at the object plane. The reconstructed phase distributions by COSHI are shown in Figs. 4(b1)–4(b3). The measurement accuracy is evaluated by the root mean square error (RMSE). The RMSEs of the results are shown below each figure in Fig. 4. The reconstructed phase distributions have some errors and the spatial structure is slightly different. It is expected that the degradation is caused by the aberration of the optical setup. Therefore, the aberration in the optical setup is measured by removing the object phase and is shown in Fig. 4(c). The results with the compensation by subtracting the aberration is shown in Figs. 4(d1)–4(d3). From the results, the error can be reduced and the measurement accuracy can be improved.

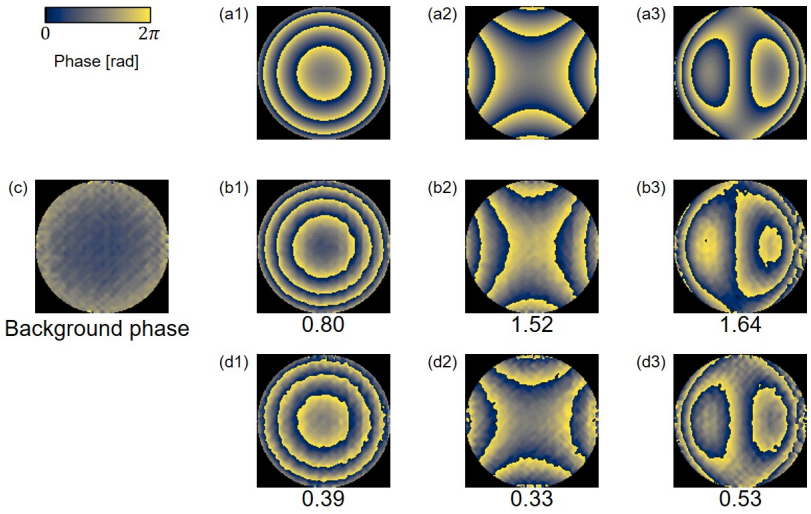

Fig. 4. (a1)-(a3) target phase, (b1)-(b3) reconstructed phase with background phase, (c) background phase, and (d1)-(d3) reconstructed phase without background phase.

A practical object was also measured using COSHI. A microdot lens was used as the target object and the structure is shown in Fig. 5(a). The microdot lens is used in the field of quantitative

Optics EXPRESS

phase imaging [16,17,42]. The microdot lens is composed of dots and gaps, with different optical path lengths. The diameter of each dot is approximately 470μm. The reconstructed phase distribution through a general Mach–Zehnder interferometer is shown in Fig. 5(b). The reconstructed phase distribution using COSHI is shown in Fig. 5(c) where the background phase shown in Fig. 4(c) is already removed. The discrepancy of the gradual background phases shown in Fig. 5(b) and 5(c) is because the measured phase distribution from each method is in a different region of the microdot lens. The results confirm that the phase difference of dots and gaps can be obtained, the practical object was measured using COSHI.

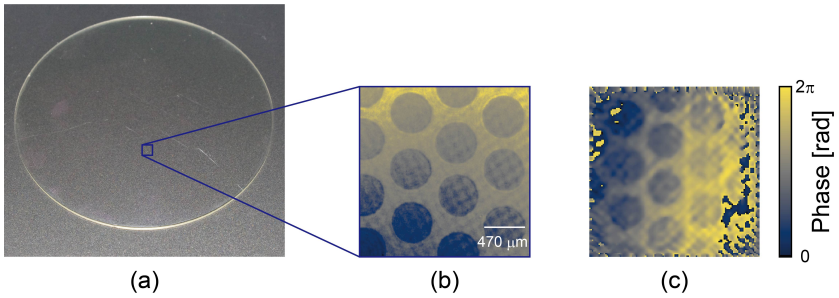

Fig. 5. (a) Microdot lens and the phase distributions reconstructed by (b) the general Mach–Zehnder interferometer and (c) COSHI.

4. Discussion

First, the approximation effect in Eqs. (7) and (8) is evaluated. The effect is described in Fig. 6 with some images. Figure 6(a) shows the images of Eq. (6). Because each term in Eqs. (6) and (8) is the complex value, the absolute values are shown in Fig. 6. As shown in Fig. 6(a), the top left images for $H(x, y)$ and $\frac{1}{N}\sum_{j=1}^{N} m_j(x, y)(I_{Sj} + I_{Rj})$ have high values, which is because the top left in the all Hadamard patterns is 1. Through the approximation in Eq. (7), $H'(x, y)$ is obtained as shown in Fig. 6(b). Since it is difficult to see the distribution of $H(x, y)$ and $\frac{1}{N}\sum_{j=1}^{N} m_j(x, y)(I_{Sj} + I_{Rj})$, the logarithms of these terms are shown in Fig. 6(c). As shown in Fig. 6(c), $\frac{1}{N}\sum_{j=1}^{N} m_j(x, y)(I_{Sj} + I_{Rj})$ has spatial distribution, which is caused by the approximation error. Although the error is superimposed on the pure interference term as $H'(x, y)$, $H'(x, y)$ has no spatial distribution of the autocorrelation term of the object $|O(x, y)|^2$; therefore, the space bandwidth of COSHI is larger than that of conventional off-axis digital holography.

Second, in COSHI, the position and size of the pinhole are important factors for the phase measurement accuracy because Eq. (2) imposes on the detector to extract the DC component. These effects are evaluated via numerical simulation. The effect of the position displacement of a single-pixel detector is evaluated. The target complex amplitude distribution is shown in Fig. 7(a). The reconstructed complex amplitude distributions when the shift size of the detector are 0 and 4$\Delta\mu$ are shown in Fig. 7(b) and 7(c), respectively; where $\Delta\mu$ indicates the size of the diffraction limit. From the results in Fig. 7(c), the displacement effects induce the multiplication of the linear phase distribution, which is easily predicted from Eq. (2).

Next, the effect of the pinhole size is evaluated. The pinhole size is set to $n \times n$ pixels and n changes from 2 to 20. The evaluation results are shown in Fig. 8. From the results, as the pinhole size increases, the phase difference gradually reduces. This is because the relationship of Eq. (2) is not satisfied. Therefore, the pinhole size must be precisely determined based on the numerical aperture of a Fourier transform lens.

Next, the space bandwidth of the typical off-axis digital holography and COSHI was numerically compared. The target object is shown in Fig. 9(a). The size of the target is the same condition as

Optics EXPRESS

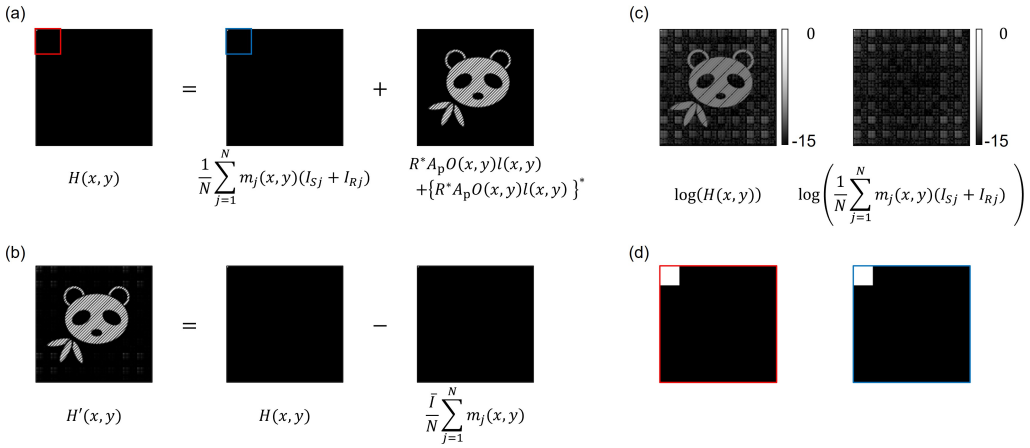

Fig. 6. Distributions of the absolute values of (a) Eq. (6), (b) Eq. (8), (c) the logarithms of $H(x,y)$ and $\frac{1}{N}\sum_{j=1}^{N} m_j(x,y)(I_{Sj}+I_{Rj})$, and (d) the expanded distributions of the top left of images framed in red and blue in (a).

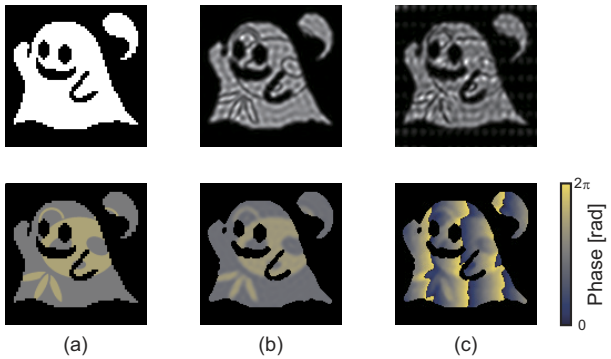

Fig. 7. (a) Target complex amplitude distribution, (b) reconstructed distributions without (b) and with

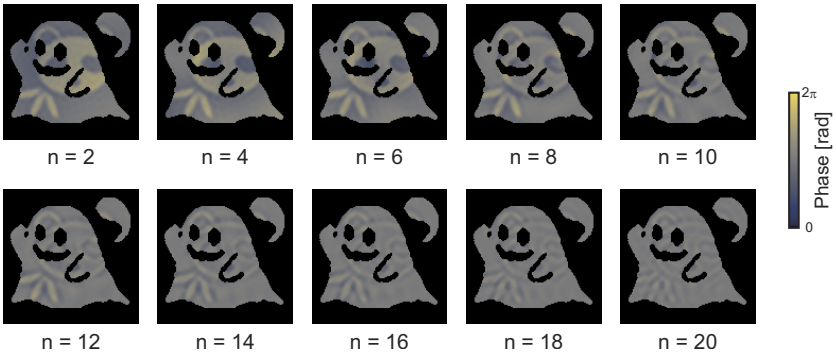

Fig. 8. Reconstructed phase distributions with various pinhole size.

Optics EXPRESS

the experiment. The tilted angle of the reference beam to the optical axis was set to 0.6°. Because the maximum angle of the reference beam satisfies the sampling condition of $1.2° = \sin^{-1}(\lambda/2\Delta x)$, where $\Delta x = 12.5\mu$m and λ =532 nm, this numerical simulation condition satisfies the sampling condition. The holograms detected by off-axis digital holography and COSHI are shown in Figs. 9(b-1) and 9(c-1), respectively. Note that the hologram detected by COSHI is a complex amplitude distribution, the absolute value of the hologram is shown in Fig. 9(c-1). The Fourier spectrum of Figs. 9(b-1) and 9(c-1) are shown in Figs. 9(b-2) and 9(c-2), respectively. Despite the result of off-axis digital holography, COSHI does not reconstruct the self-correlation term distributed in the center region in the Fourier spectrum, resulting in a larger space bandwidth than that of off-axis digital holography. The reconstructed intensity distribution through the FFA with the Fourier spectrum indicated by the highlight region in Figs. 9(b-2) and 9(c-2) are shown in Fig. 9(b-3) and 9(c-3), respectively. In the result of off-axis digital holography, the desired distribution cannot be obtained because the unnecessary components from the self-correlation term are multiplied to the one. On the other hand, COSHI clearly obtains the object distribution, making its space bandwidth larger than that of off-axis digital holography.

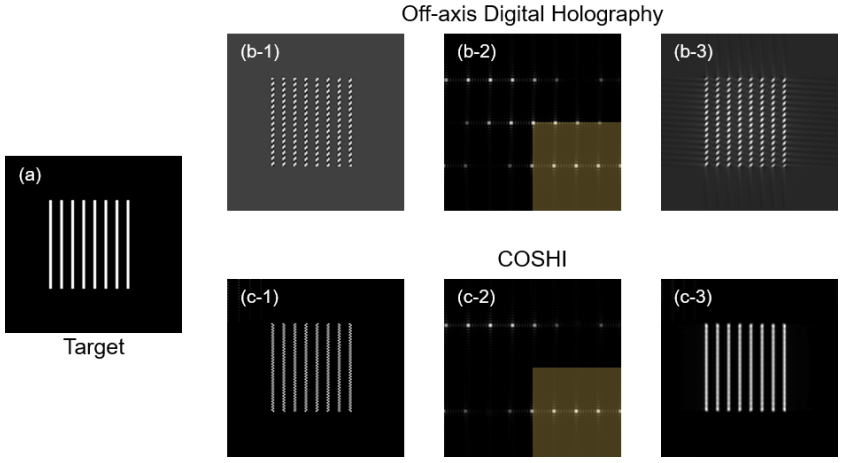

Fig. 9. Comparison results between off-axis digital holography and COSHI. (a) target object, (b) results of off-axis digital holography, (b-1) hologram, (b-2) intensity distribution of the Fourier spectrum of the hologram and (b-3) reconstructed intensity distribution. (c) results of COSHI, (c-1) absolute value of the hologram, (c-2) intensity distribution of the Fourier spectrum of the hologram and (c-3) reconstructed intensity distribution.

Notably, if the space bandwidth is limited to a quarter as shown in Fig. 10(a), the similar complex amplitude distribution can be obtained using the four-step phase-shifting method with the number of pixels of $N/4$. Therefore, under this condition, the number of measurements for COSHI is the same as the four-step phase-shifting method. In COSHI, however, as shown in Fig. 10(b), the space bandwidth along x or y axis is completely obtained by changing the tilted direction of the stationary tilt phase distribution. This asymmetric band shape is unique for COSHI, and the same space bandwidth cannot be achieved in the four-step phase-shifting method because the number of pixels in the Hadamard pattern is limited to $2^n \times 2^n$, where n is integer. In summary, although COSHI has a half space bandwidth along x or y axis, the nunber of measurements can be reduced to a quarter compared with the case of the four-step phase shifting method.

Optics EXPRESS

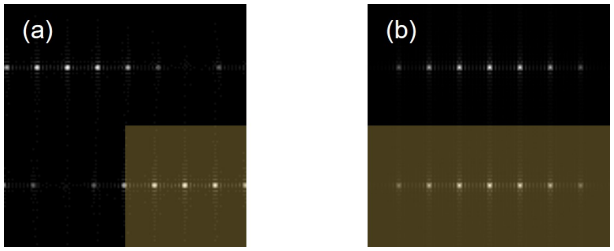

Fig. 10. Comparison of the bandwidth: (a) a quarter of the bandwidth and (b) a half of one.

5. Conclusion

In this study, COSHI was proposed to reduce the measurement time for single-pixel holographic techniques using a simple optical setup. Since the reconstruction process of COSHI is based on the FFA, the number of measurements for the phase-shifting technique can be reduced. The feasibility of the proposed method was experimentally verified. In addition, the effects of the position and size of the detector were evaluated in the numerical simulation. Since COSHI reconstructs the interference term, multiplexing techniques [43,44] which have been proposed in off-axis digital holography could be applied to the proposed method in the future. Moreover, space bandwidth could be expanded by applying Hilbert-Huang transform techniques [45,46].

Funding. Japan Society for the Promotion of Science (JP20J10441).

Acknowledgment. We thank Dr. Koshi Komuro and Mr. Chiaki Fukui for their valuable discussions and help.

Disclosures. The authors declare no conflicts of interest.

Data availability. The data that support the findings of this study are available from the corresponding author upon reasonable request.

References

1. W. K. Pratt, J. Kane, and H. C. Andrews, "Hadamard transform image coding," Proc. IEEE **57**(1), 58–68 (1969).
2. J. H. Shapiro, "Computational ghost imaging," Phys. Rev. A **78**(6), 061802 (2008).
3. Z. Zhang, X. Ma, and J. Zhong, "Single-pixel imaging by means of Fourier spectrum acquisition," Nat. Commun. **6**(1), 6225 (2015).
4. I. Hoshi, T. Shimobaba, T. Kakue, and T. Ito, "Single-pixel imaging using a recurrent neural network combined with convolutional layers," Opt. Express **28**(23), 34069–34078 (2020).
5. P. Clemente, V. Durán, V. Torres-Company, E. Tajahuerce, and J. Lancis, "Optical encryption based on computational ghost imaging," Opt. Lett. **35**(14), 2391–2393 (2010).
6. Z. Zhang and J. Zhong, "Three-dimensional single-pixel imaging with far fewer measurements than effective image pixels," Opt. Lett. **41**(11), 2497–2500 (2016).
7. N. Radwell, K. J. Mitchell, G. M. Gibson, M. P. Edgar, R. Bowman, and M. J. Padgett, "Single-pixel infrared and visible microscope," Optica **1**(5), 285–289 (2014).
8. B. I. Erkmen, "Computational ghost imaging for remote sensing," J. Opt. Soc. Am. A **29**(5), 782–789 (2012).
9. W. L. Chan, K. Charan, D. Takhar, K. F. Kelly, R. G. Baraniuk, and D. M. Mittleman, "A single-pixel terahertz imaging system based on compressed sensing," Appl. Phys. Lett. **93**(12), 121105 (2008).
10. J. Peng, M. Yao, J. Cheng, Z. Zhang, S. Li, G. Zheng, and J. Zhong, "Micro-tomography via single-pixel imaging," Opt. Express **26**(24), 31094–31105 (2018).
11. Z. Zhang, S. Jiao, M. Yao, X. Li, and J. Zhong, "Secured single-pixel broadcast imaging," Opt. Express **26**(11), 14578–14591 (2018).
12. S. Jin, W. Hui, Y. Wang, K. Huang, Q. Shi, C. Ying, D. Liu, Q. Ye, W. Zhou, and J. Tian, "Hyperspectral imaging using the single-pixel fourier transform technique," Sci. Rep. **7**(1), 45209 (2017).
13. D. Shi, S. Hu, and Y. Wang, "Polarimetric ghost imaging," Opt. Lett. **39**(5), 1231–1234 (2014).
14. M. R. Teague, "Deterministic phase retrieval: a Green's function solution," J. Opt. Soc. Am. **73**(11), 1434–1441 (1983).
15. N. Yoneda, A. Onishi, Y. Saita, K. Komuro, and T. Nomura, "Single-shot higher-order transport-of-intensity quantitative phase imaging based on computer-generated holography," Opt. Express **29**(4), 4783–4801 (2021).
16. K. Komuro, Y. Yamazaki, and T. Nomura, "Transport-of-intensity computational ghost imaging," Appl. Opt. **57**(16), 4451–4456 (2018).

Optics EXPRESS

17. T. Ito, K. Komuro, and T. Nomura, "Pupil-modulation ghost phase imaging," Appl. Opt. **60**(15), 4398–4403 (2021).
18. M. Li, L. Bian, G. Zheng, A. Maiden, Y. Liu, Y. Li, J. Suo, Q. Dai, and J. Zhang, "Single-pixel ptychography," Opt. Lett. **46**(7), 1624–1627 (2021).
19. K. Komuro, T. Nomura, and G. Barbastathis, "Deep ghost phase imaging," Appl. Opt. **59**(11), 3376–3382 (2020).
20. P. Clemente, V. Durán, E. Tajahuerce, V. Torres-Company, and J. Lancis, "Single-pixel digital ghost holography," Phys. Rev. A **86**(4), 041803 (2012).
21. T. Shirai and A. T. Friberg, "Ghost Mach–Zehnder interferometry for phase measurement with spatially incoherent light," J. Opt. **22**(4), 045604 (2020).
22. L. Martínez-León, P. Clemente, Y. Mori, V. Climent, J. Lancis, and E. Tajahuerce, "Single-pixel digital holography with phase-encoded illumination," Opt. Express **25**(5), 4975–4984 (2017).
23. Y. Endo, T. Tahara, and R. Okamoto, "Color single-pixel digital holography with a phase-encoded reference wave," Appl. Opt. **58**(34), G149–G154 (2019).
24. D. Wu, J. Luo, G. Huang, Y. Feng, X. Feng, R. Zhang, Y. Shen, and Z. Li, "Imaging biological tissue with high-throughput single-pixel compressive holography," Nat. Commun. **12**(1), 4712 (2021).
25. H. González, L. Martínez-León, F. Soldevila, M. Araiza-Esquivel, J. Lancis, and E. Tajahuerce, "High sampling rate single-pixel digital holography system employing a dmd and phase-encoded patterns," Opt. Express **26**(16), 20342–20350 (2018).
26. I. Yamaguchi and T. Zhang, "Phase-shifting digital holography," Opt. Lett. **22**(16), 1268–1270 (1997).
27. S. Shin, K. Lee, Y. Baek, and Y. Park, "Reference-free single-point holographic imaging and realization of an optical bidirectional transducer," Phys. Rev. Appl. **9**(4), 044042 (2018).
28. S. Shin, K. Lee, Z. Yaqoob, P. T. C. So, and Y. Park, "Reference-free polarization-sensitive quantitative phase imaging using single-point optical phase conjugation," Opt. Express **26**(21), 26858–26865 (2018).
29. Y. Liu, J. Suo, Y. Zhang, and Q. Dai, "Single-pixel phase and fluorescence microscope," Opt. Express **26**(25), 32451–32462 (2018).
30. K. Ota and Y. Hayasaki, "Complex-amplitude single-pixel imaging," Opt. Lett. **43**(15), 3682–3685 (2018).
31. S. Zhao, R. Liu, P. Zhang, H. Gao, and F. Li, "Fourier single-pixel reconstruction of a complex amplitude optical field," Opt. Lett. **44**(13), 3278–3281 (2019).
32. G. Indebetouw, P. Klysubun, T. Kim, and T.-C. Poon, "Imaging properties of scanning holographic microscopy," J. Opt. Soc. Am. A **17**(3), 380–390 (2000).
33. G. Indebetouw, Y. Tada, and J. Leacock, "Quantitative phase imaging with scanning holographic microscopy: an experimental assesment," BioMed Eng. OnLine **5**(1), 63 (2006).
34. J.-P. Liu, C.-H. Guo, W.-J. Hsiao, T.-C. Poon, and P. Tsang, "Coherence experiments in single-pixel digital holography," Opt. Lett. **40**(10), 2366–2369 (2015).
35. T. Shirai, T. Setälä, and A. T. Friberg, "Ghost imaging of phase objects with classical incoherent light," Phys. Rev. A **84**(4), 041801 (2011).
36. H.-Y. Hou, Y.-N. Zhao, J.-C. Han, S.-W. Cui, D.-Z. Cao, H.-C. Liu, S.-H. Zhang, and B.-L. Liang, "Complex-amplitude single-pixel imaging using coherent structured illumination," Opt. Express **29**(25), 41827–41841 (2021).
37. M. A. Cox, E. Toninelli, L. Cheng, M. J. Padgett, and A. Forbes, "A high-speed, wavelength invariant, single-pixel wavefront sensor with a digital micromirror device," IEEE Access **7**, 85860–85866 (2019).
38. M. Takeda, H. Ina, and S. Kobayashi, "Fourier-transform method of fringe-pattern analysis for computer-based topography and interferometry," J. Opt. Soc. Am. **72**(1), 156–160 (1982).
39. N. Yoneda, Y. Saita, and T. Nomura, "Motionless optical scanning holography," Opt. Lett. **45**(12), 3184–3187 (2020).
40. N. Yoneda, Y. Saita, and T. Nomura, "Spatially divided phase-shifting motionless optical scanning holography," OSA Continuum **3**(12), 3523–3535 (2020).
41. N. Yoneda, Y. Saita, and T. Nomura, "Three-dimensional fluorescence imaging through dynamic scattering media by motionless optical scanning holography," Appl. Phys. Lett. **119**(16), 161101 (2021).
42. S. Kakei, K. Komuro, and T. Nomura, "Transport-of-intensity phase imaging with polarization directed flat lenses," Appl. Opt. **59**(7), 2011–2015 (2020).
43. J. Kühn, T. Colomb, F. Montfort, F. Charrière, Y. Emery, E. Cuche, P. Marquet, and C. Depeursinge, "Real-time dual-wavelength digital holographic microscopy with a single hologram acquisition," Opt. Express **15**(12), 7231–7242 (2007).
44. C. J. Mann, P. R. Bingham, V. C. Paquit, and K. W. Tobin, "Quantitative phase imaging by three-wavelength digital holography," Opt. Express **16**(13), 9753–9764 (2008).
45. M. Trusiak, V. Mico, J. Garcia, and K. Patorski, "Quantitative phase imaging by single-shot Hilbert–Huang phase microscopy," Opt. Lett. **41**(18), 4344–4347 (2016).
46. M. Trusiak, M. Cywińska, V. Micó, J. Á. Picazo-Bueno, C. Zuo, P. Zdańkowski, and K. Patorski, "Variational Hilbert quantitative phase imaging," Sci. Rep. **10**(1), 13955 (2020).